Complex master slave interferometry

Sylvain Rivet,[1,2,*] Michael Maria,[1,3] Adrian Bradu,[1] Thomas Feuchter,[3] Lasse Leick[3] and Adrian Podoleanu[1]

[1]*Applied Optics Group, School of Physical Sciences, University of Kent, Canterbury CT2 7NH, UK*
[2]*Université de Bretagne Occidentale, EA 938 Laboratoire de Spectrométrie et Optique Laser, 6 avenue Le Gorgeu, C.S. 93837, 29238 Brest Cedex 3, France*
[3] *NKT Photonics A/S, Blokken 84, DK-3460 Birkerod, Denmark*

[*sylvain.rivet@univ-brest.fr](mailto:sylvain.rivet@univ-brest.fr)

Abstract: A general theoretical model is developed to improve the novel Spectral Domain Interferometry method denoted as Master/Slave (MS) Interferometry. In this model, two functions, *g* and *h* are introduced to describe the modulation chirp of the channeled spectrum signal due to nonlinearities in the decoding process from wavenumber to time and due to dispersion in the interferometer. The utilization of these two functions brings two major improvements to previous implementations of the MS method. A first improvement consists in reducing the number of channeled spectra necessary to be collected at Master stage. In previous MSI implementation, the number of channeled spectra at the Master stage equated the number of depths where information was selected from at the Slave stage. The paper demonstrates that two experimental channeled spectra only acquired at Master stage suffice to produce A-scans from any number of resolved depths at the Slave stage. A second improvement is the utilization of complex signal processing. Previous MSI implementations discarded the phase. Complex processing of the electrical signal determined by the channeled spectrum allows phase processing that opens several novel avenues. A first consequence of such signal processing is reduction in the random component of the phase without affecting the axial resolution. In previous MSI implementations, phase instabilities were reduced by an average over the wavenumber that led to reduction in the axial resolution.

OCIS codes: (110.4500) Optical coherence tomography; (120.3890) Medical optics instrumentation; (110.4190) Multiple imaging; (170.4460) Ophthalmic optics and devices.

References and links

1. J. Fujimoto, "Optical coherence tomography for ultrahigh resolution in vivo imaging," Nat. Biotechnol. **21**, 1361-1367 (2003).
2. D. Huang, E. A. Swanson, C. P. Lin, J. S. Schuman, W. G. Stinson, W Chang, M. R. Hee, T Flotte, K Gregory, C. A. Puliafito and J. G. Fujimoto, "Optical coherence tomography," Science **254**, 1178-1181 (1991).
3. Z. Hu and A. M. Rollins, "Fourier domain optical coherence tomography with a linear-in-wavenumber spectrometer," Opt. Lett. **32**(24), 325-327 (2007).
4. V. M. Gelikonov, G. V. Gelikonov, and P. A. Shilyagin, "Linear-wavenumber spectrometer for high-speed spectral-domain optical coherence tomography," Opt. Spectrosc. **106**(3), 459–465 (2009).
5. A. Payne and A. Gh. Podoleanu, "Direct electronic linearization for camera-based spectral domain optical coherence tomography," Opt. Lett. **37**(12), 2424-2426 (2012).
6. M. Wojtkowski, V. Srinivasan, T. Ko, J. Fujimoto, A. Kowalczyk, and J. Duker, "Ultrahigh-resolution, high-speed, Fourier domain optical coherence tomography and methods for dispersion compensation," Opt. Express **12**, 2404-2422 (2004).

7. C. C. Rosa, John Rogers, and A. Gh. Podoleanu, "Fast scanning transmissive delay line for optical coherence tomography," Opt. Lett. **30**, 3263-3265 (2005).
8. C. Yang, S. Yazdanfar and J. A. Izatt, "Fast scanning, dispersion-adjustable reference delay for OCT using fiber Bragg gratings," Proc. SPIE **5140**, 53-59 (2003).
9. Y. Yasuno, V. D. Madjarova, S. Makita, M. Akiba, A. Morosawa, C. Chong, T. Sakai, K.-P. Chan, M. Itoh, and T. Yatagai, "Three-dimensional and high-speed swept-source optical coherence tomography for in vivo investigation of human anterior eye segments," Opt. Express **13**(26), 10652–10664 (2005).
10. N. Lippok, S. Coen, P. Nielsen, and F. Vanholsbeeck, "Dispersion compensation in Fourier domain optical coherence tomography using the fractional Fourier transform," Opt. Express **20**, 23398-23413 (2012).
11. K. K. H. Chan and S. Tang, "High-speed spectral domain optical coherence tomography using non-uniform fast Fourier transform," Biomed. Opt. Express **1**(5), 1309-1319 (2010).
12. B. Hofer, B. Povazay, B. Hermann, A. Unterhuber, G. Matz, F. Hlawatsch and W. Drexler, "Signal post processing in frequency domain OCT and OCM using a filter bank approach," Proc. SPIE **6443**, 3001-3006 (2007).
13. A. Yang, F. Vanholsbeeck, S. Coen and J. Schroeder, "Chromatic dispersion compensation of an OCT system with a programmable spectral filter," Proc. SPIE **8091**, 809125 (2011).
14. Y. Watanabe and T. Itagaki, "Real-time display SD-OCT using a linear-in-wavenumber spectrometer and a graphics processing unit," Proc. SPIE **7554**, 75542S (2010).
15. A. G. Podoleanu and A. Bradu, "Master-slave interferometry for parallel spectral domain interferometry sensing and versatile 3D optical coherence tomography," Opt. Express **21**(16), 19324–19338 (2013).
16. A. Bradu and A. G. Podoleanu, "Calibration-free B-scan images produced by master/slave optical coherence tomography," Opt. Lett. **39**(3), 450–453 (2014).
17. A. Bradu, K. Kapinchev, F. Barnes, and A. Podoleanu, "Master slave *en-face* OCT/SLO," Biomed. Opt. Express **6**, 3655-3669 (2015).
18. A. Bradu, K. Kapinchev, F. Barnes, and A. Podoleanu, "On the possibility of producing true real-time retinal cross-sectional images using a graphics processing unit enhanced master-slave optical coherence tomography system," J. Biomed. Opt. **20**(7), 076008 (2015).
19. A. Bradu, M. Maria, and A. Podoleanu, "Demonstration of tolerance to dispersion of master/slave interferometry," Opt. Express **23**(11), 14148-14161 (2015).
20. A. Bradu and A. G. Podoleanu, "Imaging the eye fundus with real-time en-face spectral domain optical coherence tomography," Biomed. Opt. Express **5**(4), 1233–1249 (2014).
21. J. Wang, A. Bradu, G. Dobre, and A. Podoleanu, "Full-field swept source master slave optical coherence tomography," IEEE Photonics Journal **7**(4), 1943-0655 (2015).

1. Introduction

Spectral (or Fourier) domain Interferometry (SDI) is widely spread in many fields of biomedical optics, especially in Optical Coherence Tomography (OCT) [1-2]. SDI encodes distances, thicknesses, scattering properties or refractive indices onto the density of modulation of the optical spectrum, *i.e.* channeled spectrum, at the interferometer output.

To decode the channeled spectrum, SDI uses a Fourier Transform (FT) operation that translates the modulation density into a distance measurement. SDI principles can be applied to systems employing either a broadband optical source (spectrometer based, Sp) or a tunable optical source (swept source, SS). In the case of a Sp system, the channeled spectrum at the interferometer output is read by a camera incorporated within the spectrometer. This channeled spectrum is chirped due to a nonlinear dependence of the pixel position in the camera versus the optical frequency. When a SS system is employed, the temporal signal read by a photodetector at the interferometer output presents a chirp mainly due to non-linear frequency sweeping. We will refer to these chirping effects as due to the decoding process from channeled spectrum. In addition to the chirp due to spectrum decoding, unbalanced dispersion in the interferometer arms also affects the regularity of maxima and minima in the readout channeled spectrum. For a strictly periodic modulation (no chirp) of the channeled spectrum, a FT returns a well-defined peak. The chirp in the spectrum modulation translates into an enlargement and reduction in the amplitude of such a peak, worsening the axial resolution and sensitivity.

In order to correct the chirping before FT, hardware and software methods have been reported. In terms of hardware solutions, a spectrometer using a prism after the diffraction

grating [3,4], or chirped sampling using an analogue line scan camera [5] were proposed. Several solutions have also been proposed to compensate for dispersion, using matched lengths of glass [6], spectral delay line [7], fiber Bragg gratings [8]. In terms of software solutions, several methods have also been developed to resample and organize the data linearly along the optical frequency axis, or wavenumber, prior to the FT. Common corrections are based on the interpolation of the phase in order to obtain linearity in k-space [9]. More complex techniques based on fractional Fourier transforms [10], non-uniform Fourier Transformation [11], or advanced computational algorithms [12-14] provide a posteriori data resampling.

Master-Slave Interferometry (MSI) is a new approach to SDI to eliminate the chirp effects [15]. The MSI proceeds in two stages. In a first stage (Master), a mirror is used as an object and experimental channeled spectra (CS_{exp}) are measured and stored, for a number P of different values of the optical path difference (OPD) in the interferometer. In a second stage (Slave), the object replaces the mirror and the channeled spectrum is compared with every CS_{exp} saved in the memory block and used as a mask. The comparison operation of each mask with the channeled spectrum was implemented via correlation [15-19] or by simplified dot product procedures for faster implementation of correlation for argument zero [20,21]. The maximum value of each comparison (correlation) is selected to provide the depth information profile (A-scan) at each OPD value selected during the Master stage.

MSI presents several advantages compared to conventional SDI. The process of data resampling performed during measurements is replaced by data storage at the Master stage, which shortens processing time while performing measurements. The quality of data resampling for the conventional FT-based method affects the axial resolution. Advantageously, MSI exhibits a constant resolution over the OPD range which recommends it as a useful tool for metrology and imaging. Each CS_{exp} provides direct access to measurements from that OPD value used at the Master stage to produce it, conferring advantage to MSI in terms of production of *en-face* OCT images. Recently, its tolerance to dispersion in the interferometer has also been demonstrated [19].

Nevertheless, the implementation of MSI reported in previous reports presents some shortcomings, such as:

(i) Typically, a large number of CS_{exp} need to be recorded at the Master stage, a problem especially when using large bandwidth sources. The sampling of the A-scans in depth is determined by the number of CS_{exp} recorded for incremental depths.

(ii) MSI is characterized by a trade-off between phase instability and axial resolution. The phase in the interferometer varies between the step of recording the CS_{exp} and the step of scanning the object to be imaged, considered here as a random phase shift φ_{rand}. As the phase is discarded, it is not possible to eliminate its effects. To reduce the effect of the random phase shift, the correlation function is averaged over several lags [15-19] that leads to some deterioration of the axial resolution.

In this paper, an improved method is presented that addresses the above shortcomings. This method, Complex Master Slave Interferometry (CMSI), does not directly use CS_{exp} as masks, contrary to [15-21], but develops a procedure to infer any number of masks from a reduced number of CS_{exp} acquired. Additionally, the masks generated are complex in order to conserve the phase information.

This paper is organized into three theoretical sections and an experimental section. The theoretical sections describe the interferometric signal in a SDI set-up unbalanced from the point of view of dispersion and equipped with a chirped decoder, obtained in conventional MSI [15-21] and in the novel CMSI presented here. The chirp affecting the channeled spectrum at the interferometer output is modeled by two functions g and h. Based on these functions, a procedure of inferring a number of Q channeled spectra (masks) at the Slave stage from a variable number P of CS_{exp}, with $Q{>>}P$ is then presented. The experimental section

demonstrates the conservation of axial resolution over depth for both spectrometer and swept source based SDI methods.

2. Chirped decoder and interferometer with unbalanced dispersion

2.1. General description of an SDI experimental set-up

In Fig. 1, a SDI schematic diagram is shown, made of two main components, an interferometer and a decoder. The interferometer includes a splitter (shown as a directional coupler), a reference mirror (M), an interface optics that conveys light towards an object (O) subject to tests or imaging. In case the application is spectral domain OCT, the interface optics contains a lateral or transversal galvo-scanner. The decoder block translates the channeled spectrum shape at the interferometer output into an electrical signal. For a spectrometer-based configuration, the source is broadband and the decoder is a spectrometer. For a swept source configuration, the optical source is a swept source laser and the decoder is a fast photodetector.
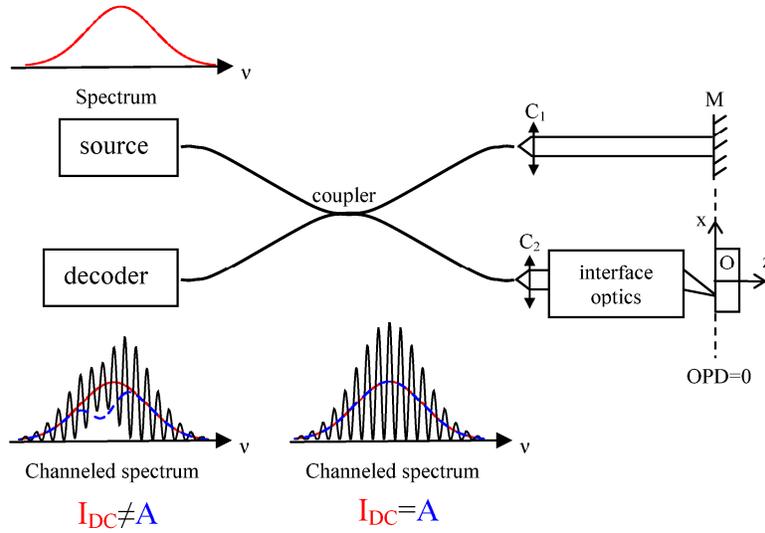
Fig. 1. Block diagram for a spectral domain OCT system. C1 and C2, collimators; M, reference mirror; O, object. Two channeled spectra are shown underneath, for a mirror as a sample. I_{DC} represents the power spectrum of the optical source, shown by the red Gaussian shape solid line. The A shape is shown by the dashed blue line, determined by the interference contrast of the modulating signal proportional to the channeled spectrum. On the left, the usual case in practice is shown when $I_{DC} \neq A$. Here, the interference contrast A is deliberately shown smaller on the left side of the spectrum. In this case, A varies below I_{DC} on the left hand side and regains the I_{DC} value on the right. The channeled spectrum on the right shows the ideal case, when $I_{DC} = A$, i.e. when the contrast profile A and the I_{DC} profile are superposed on each other.

In the following, a mathematical expression of the electrical signal at the output of the interferometer shown in Fig. 1 is obtained, where the decoder performs nonlinearly and dispersion is left unbalanced between the arms of the interferometer.

2.2. Fourier transform of the channeled spectrum

Let us consider a non-uniform distribution of frequencies $\tilde{\nu}$ along the pixels of the line array detector when using a spectrometer, or along time when using a tunable laser. The relationship between the optical frequency ν and $\tilde{\nu}$ is given by the function $g(\tilde{\nu}) = \nu$.

The unbalanced dispersion between the arms of the interferometer can be described by a function $d(\nu)$:

$$d(\nu) = \frac{2\pi}{c}\nu\left[\left(n_2(\nu) - n_2(\nu_0)\right)e_2 - \left(n_1(\nu) - n_1(\nu_0)\right)e_1\right], \qquad (1)$$

where n_1, and n_2 are the refractive indices of the dispersive parts in the reference and in the object arm respectively, e_1 and e_2 their thicknesses and ν_0 the central optical frequency of the source.

The electrical signal $I(\tilde{\nu})$ delivered by a non-ideal decoder is a chirped signal according to $\tilde{\nu}$ and can be written as a superposition of a DC term, I_{DC}, and a complex exponential form of a periodic function $\underline{I}(\tilde{\nu})$ as follows

$$I(\tilde{\nu}) = I_{DC}(g(\tilde{\nu})) + \frac{1}{2}\left(\underline{I}(\tilde{\nu}) + \underline{I}^*(\tilde{\nu})\right), \qquad (2)$$

where g takes into account the decoding procedure chirp and * corresponds to its complex conjugate. I_{DC} follows the shape of the power spectrum of the optical source (in spectrometer-based configurations and to the tuning bandwidth in swept source configurations).

Considering r the complex reflectivity of the object varying with depth ρ, the complex electrical signal $\underline{I}(\tilde{\nu})$ corresponding to the decoded channeled spectrum can be written as a continuous summation of modulations

$$\underline{I}(\tilde{\nu}) = \int r(\rho)A\left(g(\tilde{\nu})\right)Exp\left[i\left(\frac{2\pi}{c}g(\tilde{\nu})2\rho + h(\tilde{\nu})\right)\right]d\rho, \qquad (3)$$

where c is the speed of light, $h(\tilde{\nu}) = d(g(\tilde{\nu}))$ is a function depending on the unbalanced dispersion in the interferometer and the nonlinear dependence on $\tilde{\nu}$. The depth $\rho = 0$ corresponds to the OPD = 0 in the interferometer. $A(\nu)$ represents the interference contrast. In practice, $A(\nu)$ is different from the power spectrum of the optical source, $I_{DC}(\nu)$ as shown by the left channeled spectrum in Fig. 1. This is due to several additional effects such as polarization mismatching of reference light and object light fields or due to chromatic aberrations introduced by optical components, factors that reduce the axial resolution. Although the amount of unbalanced dispersion due to the object can be incorporated into the overall unbalanced dispersion present within the system, we restrict h to describe the dispersion in the interferometer only. Equation (3) presents the most general expression for the channeled spectrum, which includes the nonlinear dependence on $\tilde{\nu}$ and the dispersion effects.

If the decoder is linear ($g(\tilde{\nu}) = \tilde{\nu} = \nu$) and the interferometer is perfectly balanced for dispersion ($d \equiv 0$), the inverse Fourier transform of I is directly related to the complex reflectivity r in depth z of the object (A-scan) via the following expression as detailed in Appendix A:

$$\hat{I}\left(\frac{2z}{c}\right) = \hat{I}_{DC}\left(\frac{2z}{c}\right) + \frac{1}{2}r(z) \otimes P_0\left(\frac{2z}{c}\right) + \frac{1}{2}r(-z)^* \otimes P_0\left(-\frac{2z}{c}\right)^*, \qquad (4)$$

where $\hat{I}$ and $\hat{I}_{DC}$ are the inverse FT of I and I_{DC} respectively, $\otimes$ is the convolution operation and P_0 is the axial Point Spread Function (PSF) of the system defined by

$$P_0(t) = FT^{-1}\left[A(\nu)\right]. \qquad (5)$$

As shown by Eq. (5), the axial resolution (the width of P_0) does not vary with depth, being only determined by the interference contrast, $A(\nu)$. This happens in the case of a perfectly dispersion-balanced interferometer interrogated by an ideal decoder (either spectrometer or tuning laser).

In the paper the refractive index and the dispersion of the sample are ignored to simplify the study. All distances are measured in air. In the common practice of conventional FT based OCT methods, the depth in the sample was inferred by dividing the axial depth interval, after

FT, by the index of refraction of the sample. To compensate sample dispersion, a slab of similar material in the reference arm or a numerical compensation should be used. Similarly, the axial intervals associated to each mask of CMSI are measured in air, therefore they correspond to a depth in the sample obtained by their division to an average index of refraction. As far as sample dispersion is concerned, CMSI should also be used with a slab of similar material in the reference arm or with masks modified by the amount of dispersion to be compensated at each depth.

3. Theory of master-slave interferometry

3.1 Master slave signal

In contrast to conventional spectral (Fourier) domain interferometry, MSI delivers a signal from a single depth, z, within the object to be investigated. Initially, for the comparison operation required by the MSI method, correlation was used [15-19]. To improve on the calculation speed, a modified correlation operation was proposed [20-21], reduced to the correlation calculation in lag $\tilde{N} = 0$. This delivers the value of an A-scan at depth z, the MSI signal, according to

$$ MSI(z) = \left[C(\tilde{N}, z) \right]_{\tilde{N}=0} = \left[\int CS_{\exp} \left(\tilde{\nu} + \tilde{N}, z \right) I(\tilde{\nu}) d\tilde{\nu} \right]_{\tilde{N}=0}, \tag{6} $$

where C is the correlation operation between the channeled spectrum I collected when the object is placed in the object arm (Slave stage), and the mask corresponding to the channeled spectrum CS_{exp} collected at the Master stage for an OPD $= 2z$, when the mirror is used as an object.

3.2. Limitations in the MSI practice due to using the CS_{exp} as masks

The experimental channeled spectra $CS_{exp}(z)$ can be written according to

(i) a random phase shift $\varphi_{rand}(z)$ induced by the fluctuations of the OPD between the step of acquiring the channeled spectra to be used as masks and the step of measuring the channeled spectrum I associated to the object,

(ii) a coefficient $\alpha(z)$ describing the variation with OPD of the strength of the CS_{exp} collected. This is due for instance to the variation of the amount of light injected into single mode fibers when altering the OPD in the interferometer,

(iii) a complex-valued channeled spectrum $\underline{CS}$, not affected by the random phase shift. The channeled spectrum $\underline{CS}$ is only affected by the specific modality of decoding the spectrum into an output electric signal, and the dispersion in the interferometer as follows:

$$ \underline{CS}(\tilde{\nu}, z) = A\big(g(\tilde{\nu})\big) Exp\left[i\left(\frac{2\pi}{c} g(\tilde{\nu}) 2z + h(\tilde{\nu}) \right) \right]. \tag{7} $$

According to the considerations (i), (ii) and (iii) above, the experimental channeled spectrum is described by

$$ CS_{\exp}(\tilde{\nu}, z) = \frac{1}{2}\alpha(z)\, \underline{CS}(\tilde{\nu}, z) e^{i\varphi_{rand}(z)} + \frac{1}{2}\alpha(z)\, \underline{CS}(\tilde{\nu}, z)^* e^{-i\varphi_{rand}(z)}. \tag{8} $$

Note that no DC component appears in Eq. (8) because a high-pass filter is applied on each saved CS_{exp}.

Combining Eqs. (6)-(8), the MSI signal can be written as

$$ MSI(z) = \frac{1}{2}\alpha(z) e^{-i\varphi_{rand}(z)} \int \underline{CS}(\tilde{\nu}, z)^* \, I(\tilde{\nu}) d\tilde{\nu} + CC, \tag{9} $$

where CC stands for Complex Conjugate, or using the complex exponential form of $\underline{I}$ (Appendix B), as

$$ MSI(z) = \frac{1}{2}\Re e\left\{ \alpha(z) e^{-i\varphi_{rand}(z)} \int \underline{CS}(\tilde{\nu}, z)^* \, \underline{I}(\tilde{\nu}) d\tilde{\nu} \right\}, \tag{10} $$

where $Re\{\}$ denotes the real part of the complex function within the curly brackets. Equation (10) is valid for an object positioned outside OPD = 0 (Appendix B).

In order to present the relationship between the MSI signal and the reflectivity r of the object, a complex function $\gamma(z)$ is defined by

$$\gamma(z) = \int \underline{CS}(\tilde{v},z)^{*} \, \underline{I}(\tilde{v})d\tilde{v} . \qquad (11)$$

Using the expression of the $\underline{CS}$ given by Eq. (7) and the expression of the complex channeled spectrum $\underline{I}$ given by Eq. (3), $\gamma(z)$ can be expressed as

$$\gamma(z) = \iint r(\rho) \left| A(g(\tilde{v})) \right|^{2} Exp\left[-i\left(\frac{2\pi}{c} g(\tilde{v}) \times 2(z-\rho)\right)\right] d\rho \, d\tilde{v} . \qquad (12)$$

As the same amount of unbalanced dispersion $h(\tilde{v})$ is present in both CS_{exp} and I, (and consequently in their complex forms $\underline{CS_{exp}}$ and $\underline{I}$), the effect of unbalanced dispersion is totally eliminated in Eq. (12). A change of variable, $\delta = z\text{-}\rho$, allows us to rewrite Eq. (12) as

$$\gamma(z) = \iint r(z-\delta) \left| A(g(\tilde{v})) \right|^{2} exp\left[-i\left(\frac{2\pi}{c} g(\tilde{v})2\delta\right)\right] d\delta \, d\tilde{v} . \qquad (13)$$

Let us denote P_I as

$$P_1(t) = \int \left| A(g(\tilde{v})) \right|^{2} Exp\left[-i\,2\pi\, g(\tilde{v})t\right]d\tilde{v} . \qquad (14)$$

In case $g(\tilde{v}) = \tilde{v} = v$, we recognize $P_1(t)$ as the axial PSF of the system, similar to Eq. (5). Here the power of the interference contrast A is squared because both the masks CS_{exp} and I depend on A. Using Eq. (14) in Eq. (13), $\gamma(z)$ can be expressed as a convolution product between the complex reflectivity profile of the object $r(z)$ and the function $P_I(2z/c)$:

$$\gamma(z) = \int r(z-\delta) P_1(2\delta/c) \, d\delta = r(z) \otimes P_1(2z/c), \qquad (15)$$

Let us consider G as the inverse function of g, $G(g) \equiv 1$. Using a change of variable $g(\tilde{v}) = v$, the function P_I can be expressed as follows

$$P_1(t) = \int \left| A(v) \right|^{2} Exp[-ivt]G'(v)dv , \qquad (16a)$$

where $G'(v)$ is the derivative of $G(v)$ in respect to v. Via a Fourier transform, Eq. (16a) can be written as

$$P_1(t) = FT^{-1}\left[\left| A(v) \right|^{2} G'(v)\right]. \qquad (16b)$$

As a more general description for the MSI operation, the MSI signal for OPD = $2z$ can be expressed as the convolution product between the depth-resolved complex reflectivity r and the axial PSF P_1, defined in Eq. (16b), by

$$MSI(z) = \frac{\alpha(z)}{2}\Re e\left\{e^{i\varphi_{rand(z)}} \left(r(z) \otimes P_1(2z/c)\right)\right\} . \qquad (17)$$

Eq. (17) shows that the reflectivity of the sample measured via the MSI method is independent of the amount of dispersion left unbalanced, meaning that the axial resolution is not affected. This property has already been demonstrated in [19]. Additionally, as the decoding non-linearity described by G' is the same at all OPD values, the axial resolution is also independent on z but it is not optimal, as Eq. (16b) involves the square of A than simply A in Eq. (5). For instance if A has a Gaussian shape, the axial resolution is $\sqrt{2}$ poorer than the axial resolution obtained with the FT method without any unbalanced dispersion and nonlinearities. An improvement in the practice of MSI would be to eliminate the shape of A from the masks in Eq. (10) as suggested by the theoretical model in [19] but not done in [15-18,20,21]. Equation (17) also shows that combination of phase in the complex r with the random phase impedes the recovery of the complex r.

In order to address this problem, we propose to use complex masks, as we describe in the next section.

4. Complex master-slave interferometry

The main idea of CMSI is to generate, during the Master stage, a complex function incorporating two phenomena: (i) the non-uniform distribution along the axis, $\tilde{v}$, of the detector (pixel for spectrometer or time slot for swept source) due to the nonlinearities in the decoder, function g, and (ii) the unbalanced dispersion of the interferometer, function h. The masks to be used in CMSI at the Slave stage are then to be obtained from this complex function, evaluated in as many OPD = $2z$ values as the user requires, independently from the OPD values used to measure the CS_{exp}.

4.1 Extraction of the functions g($\tilde{v}$) and h($\tilde{v}$) at the master stage

In CMSI, it is possible to infer the masks from a Mask function M_{built} created by calculating the functions $g(\tilde{v})$ and $h(\tilde{v})$ from data acquired in the Master stage, when a number P of CS_{exp} are recorded for P OPD values. These experimental channeled spectra are then extended into their complex exponential form $\underline{CS}_{exp}$ according to a procedure described in Appendix C and in Fig. 11. Their corresponding phases $\phi^{exp}(\tilde{v}, z)$ are obtained by extracting the arguments of $\underline{CS}_{exp}$. The phase $\phi^{exp}(\tilde{v}, z)$ is expressed according to

$$\phi^{exp}(\tilde{v},z) = \frac{2\pi}{c} g(\tilde{v})\, 2z + h(\tilde{v}) + \varphi_{rand}(z)\,. \tag{18}$$

A partial derivative of Eq. (18) in respect to $\tilde{v}$ removes the random phase and leads to

$$\frac{\partial}{\partial \tilde{v}}\phi^{exp}(\tilde{v},z) = \frac{2\pi}{c} g'(\tilde{v})\, 2z + h'(\tilde{v})\,, \tag{19}$$

where $g'(\tilde{v})$ and $h'(\tilde{v})$ are the derivatives of $g(\tilde{v})$ and $h(\tilde{v})$.

A linear regression according to z permits to retrieve the slope $4\pi g'(\tilde{v}_i)/c$ and the y-intercept $h'(\tilde{v}_i)$ for each $\tilde{v}_i$ of the channeled spectrum, and build $4\pi g'(\tilde{v})/c$ and $h'(\tilde{v})$ along the spectral coordinate $\tilde{v}$. Then an indefinite integration is used to infer $4\pi g(\tilde{v})/c$ and $h(\tilde{v})$. Figure 2 describes the step by step procedure of obtaining the set of functions g and h from an experimental set of CS_{exp}, and then the Mask function M_{built}.
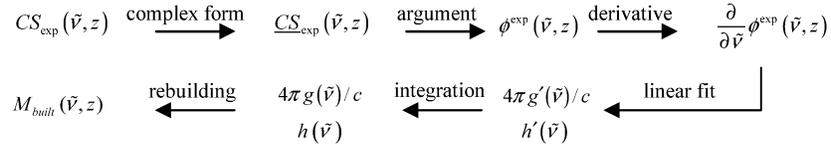
Fig. 2. Step by step procedure to infer the Mask function from a reduced set of experimentally measured channeled spectra.

By retaining the phase of the CS_{exp} only, the spectral amplitude of the Mask functions M_{built} is flat. The elimination of the spectral dependence of the masks used by CMSI leads to an optimum axial resolution related to $FT^{-1}[A]$ as it will be demonstrated in Section 4.3 below.

4.2 Complex MSI signal

The Mask function M_{built} to be used by the CMSI, is defined at the OPD = $2z$ as

$$M_{built}(\tilde{v},z) = g'(\tilde{v})\, Exp\left[i\left(\frac{2\pi}{c} g(\tilde{v})2z + h(\tilde{v})\right)\right]\,, \tag{20}$$

where $g'(\tilde{v})$ is the derivative of $g(\tilde{v})$. CMSI signal is defined similarly to Eq. (6) by the following integral

$$\text{CMSI}(z) = \int M_{built}^*(\tilde{v},z)\, I(\tilde{v})\,d\tilde{v}\,. \tag{21}$$

CMSI involves a similar definition to the MSI except that the CS_{exp} used as masks are replaced by a complex function with the adjustable parameter z. CMSI is valid for an object set outside OPD = 0, *i.e.* $2z$ should be larger than the coherence length L_c of the light source (inverse proportional to the bandwidth of the optical source in Sp-OCT and to the tuning bandwidth in SS-OCT).

4.3 Relation between CMSI and reflectivity r in depth

By using the complex exponential form of I, CMSI can be written as follows (Appendix D)

$$\text{CMSI}(z) = \frac{1}{2}\int M_{built}^*(\tilde{v},z)\ \underline{I}(\tilde{v})\,d\tilde{v}, \tag{22}$$

and the operation of the CMSI can be described by

$$\text{CMSI}(z) = \frac{1}{2}\iint r(\rho)\ A\big(g(\tilde{v})\big)\ Exp\left[-i\left(\frac{2\pi}{c}g(\tilde{v})\times 2(z-\rho)\right)\right] g'(\tilde{v})\,d\tilde{v}\,d\rho, \tag{23}$$

according to Eq. (20) and Eq. (3). Changes of variable $v = g(\tilde{v})$ and $\delta = z\text{-}\rho$ are carried out in Eq. (23) leading to

$$\text{CMSI}(z) = \frac{1}{2}\iint r(z-\delta)\ A(v)\ Exp\left[-i\frac{2\pi}{c}v\,2\delta\right]dv\,d\delta. \tag{24}$$

Equation (24) can be rewritten as a convolution product between the complex reflectivity profile $r(z)$ and the point spread function P_0

$$\text{CMSI}(z) = \frac{1}{2}r(z)\otimes P_0\left(2z/c\right), \tag{25}$$

for $2z>L_c$ where P_0 is the axial PSF defined by Eq. (5) and equal to FT^{-1}[A].

Again, depth information profile is extracted and expressed as a convolution product between a complex reflectivity function and the ideal PSF of the system, which leads to a constant axial resolution in depth irrespective of the non-linearity of the decoder and irrespective of the amount of the unbalanced dispersion in the interferometer.

The drawbacks of the previous implementations of MSI addressed by CMSI are: (i) the depth points of the A-scan are now determined by a sampling parameter z, independent of the OPD values used to acquire the CS_{exp} in the Master stage, (ii) CMSI operation returns a complex signal, hence phase of r is conserved. Moreover, the building of the Mask function does not depend on the random phase shift as it will be shown in Section 5, which eliminates the need for averaging over an interval of lag wavenumbers (window in [15-19], practiced in previous MSI reports). (iii) The axial resolution is related to FT^{-1}[A], as for a perfect interferometer.

5. Experimental results

5.1 Discrete formulation of the CMSI operation

As with the MSI, CMSI has been described above by continuous variables, however practical implementations involve digital processing. Let $M_{built}(n, q)$ be the complex mask inferred at the Master stage, where $n = 1$ to N corresponds to the sampling along the pixels in the spectrometer line camera or along the time slots within the sweeping time for a swept source and where $q = 1$ to Q corresponds to the different OPDs required by the user independently from the P number of CS_{exp}. In these conditions, Eq. (20) becomes

$$M_{built}(n,q) = g'(n)\ Exp\left[i\left(\frac{2\pi}{c}g(n)q\,\Delta OPD + h(n)\right)\right], \tag{26}$$

where ΔOPD defined by the user is, in practice, at least half of the coherence length of the optical source, and Eq. (21) can be re-written as

$$\text{CMSI}(q) = \sum_{n=1}^{N} M_{built}^{*}(n,q)\, I(n)\,, \tag{27}$$

as an upgrade of the dot product introduced in [19]. In this way, an A-scan can be assembled from CMSI signals evaluated at Q depths, given by the number of Q masks inferred from the number P of the CS_{exp} acquired at the Master stage.

The operation of the CMSI is demonstrated below on two versions of the set-ups described in Fig. 1, in Section 5.2 using a broadband source and a spectrometer and in Section 5.3 using a swept source and a photodetector.

5.2 A-scan with a spectrometer-based OCT

The experimental set-up is similar to that shown in [16,19]. The broadband source is a super Luminescent Diode (SLD) with a Gaussian spectrum centered at 1306±2 nm and a bandwidth of 28±1nm. The detection part includes a home-built spectrometer equipped with an InGaAs linear camera (Goodrich SUI, Princeton, New-Jersey, model SU-LDH, 1024 pixels, 14-Bit). Data obtained from the system are directly processed by the CMSI procedure with no resampling.

At the Master stage, experimental channeled spectra are recorded for different values of the OPD. After the extraction of the experimental phases (procedure presented in Section 4.1), the variation of $\partial\phi^{\text{exp}}/\partial\tilde{v}$ according to the position of the mirror, looks like the one presented at the center of the spectrum $\tilde{v}_{c}$ (Fig. 3).

The linear regression on the derivative of the experimental phase for each value of $\tilde{v}$ permits to extract the functions $g(\tilde{v})$ and $h(\tilde{v})$. The integration constant has been chosen so that $g(\tilde{v})$ and $h(\tilde{v})$ are equal to zero at the center of the spectrum.

Figures 4(a) and 4(b) show $g(\tilde{v})$ and $h(\tilde{v})$ calculated from three sets of limited number P of CS_{exp}. These sets correspond to $P = 2$, $P = 11$ and $P = 71$ of CS_{exp} recorded from $z = 140$ μm to $z = 1540$ μm at the Master stage. The accuracy of determining g and h depends on the noise of the experimental phase measurement and the number of points, *i.e.* the number P of CS_{exp}, used for the linear regression. In the case of this experiment, the functions g and h inferred are quite similar for the three sets of CS_{exp}, as shown in Fig. 4. The instabilities shown at the edges of the spectrometer do not count in practice, as the optical spectrum is almost zero there, shown in solid line.
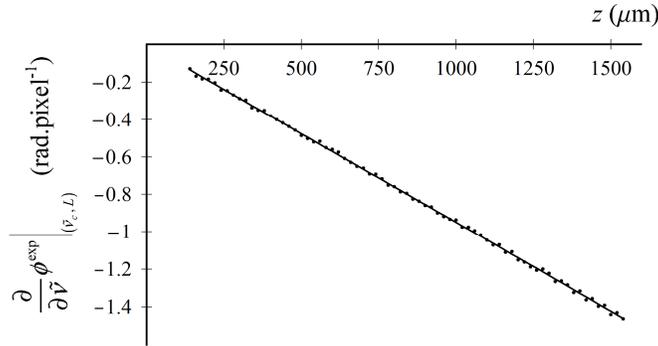
Fig. 3. Derivative of the experimental phase with respect to $\tilde{v}$ for different positions of the reference mirror M in Fig. 1 (black dots) adjusting the OPD = 2z. The derivative phase is evaluated at the center of the spectrum $\tilde{v}_{c}$. Continuous line, linear fit of experimental measurements.
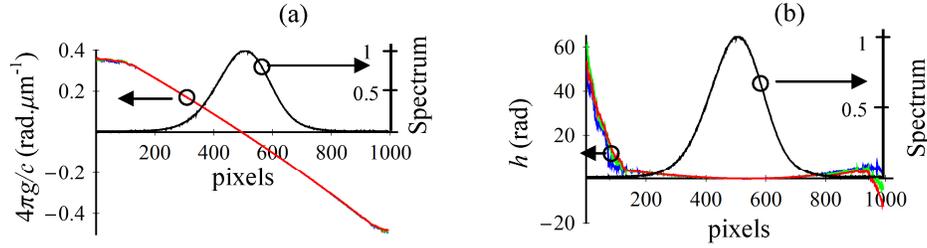
Fig. 4. The functions g (a) and h (b) versus the pixels of the spectrometer according to the number P of CS_{exp} acquired in the Master stage. Blue line, $P = 2$. Green line, $P = 11$. Red line, $P = 71$. Black line, normalized channeled spectrum at the Master stage for OPD = 0.

At the Slave stage, channeled spectra have been recorded for 3 positions of the reference mirror (220 µm, 720 µm and 1320 µm measured from OPD = 0). Figure 5 shows the axial reflectance profile based on Fourier Transform (black line) and CMSI according to the three sets of CS_{exp} (blue line for $P = 2$, green line for $P = 11$ and red line for $P = 71$). An axial sampling of 2 µm was chosen for CMSI to perform good sampling of the A-scan peaks, *i.e.* using $Q = 771$ masks in the range [0, 1540 µm]. The Fourier transformation of the channeled spectrum for 3 positions of the reference mirror is calculated to demonstrate the existence of chirp in the channelled spectra.
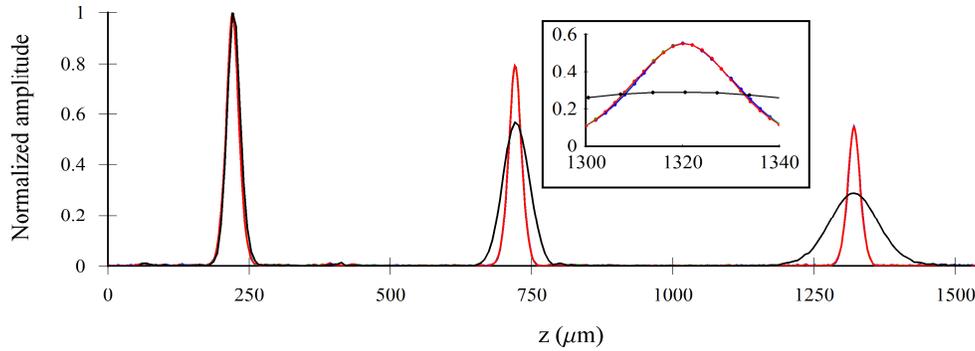
Fig. 5. A-scans for 3 OPD = 2z values ($z = 220$ µm, 720 µm and 1320 µm measured from OPD=0). Black line, A-scan peaks obtained using FT. Blue line, A-scans obtained using CMSI with $P=2$ CS_{exp} in the Master stage. Green line, A-scans obtained using CMSI with $P = 11$. Red line, A-scans obtained using CMSI with $P = 71$. All peaks are normalized with respect to the first peaks at $z = 220$ µm. The inset shows a zoom in the peaks around 1320 µm.

Although FT peaks broaden with OPD due to the dispersion induced by the interferometer and the non-linearity of spectral conversion in the spectrometer, the peak width of CMSI does not change with depth. Moreover, the reflectance profiles are identical irrespective of the number of CS_{exp} used for inferring the Mask function M_{built}. The graphs in Fig. 5 show that high resolution A-scans are achievable with a mask M_{built} obtained from $P = 2$ CS_{exp} only. Lastly, the inset of Fig. 5 shows details in the peaks around 1320 µm and the fact that the profiles for $P = 2$, 11 and 77 are identical.

Obviously, if a resampling method would be used, then the FT profile would be narrowed and in principle, if such resampling/linearization would be done to perfection, the ideal shape of A-scan peaks should be obtained as well. We do not show such graphs here as they have been presented in numerous reports on the conventional FT based OCT and such corrections are not the subject of this study.
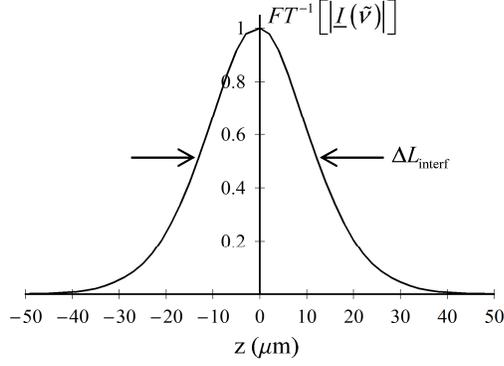
Fig. 6. PSF corresponding to the channeled spectrum I for the OPD at position 3 (z = 1340 μm) in Fig. 5. The PSF is obtained by calculating FT^{-1}[$|\underline{I}(\tilde{\nu})|$] that is equal to FT^{-1}[$|A(g(\tilde{\nu}))|$]. The complex form $\underline{I}$ has been calculated in Appendix C. FT^{-1}[$|\underline{I}(\tilde{\nu})|$] corresponds to the Fourier transformation of a channeled spectrum with no chirp.

It is important to distinguish two modalities to evaluate the axial resolution: 1) ΔL_{DC} equal to the full width at half maximum (FWHM) of the FT^{-1}[$I_{DC}(g(\tilde{\nu}))$] profile. For a Gaussian spectrum shape the axial resolution is mathematically described by $\Delta L_{DC} = (2\text{Ln2})/\pi \times \lambda_c^2/\Delta\lambda = 27\pm1$ μm, which represents the ideal axial resolution, determined by the source bandwidth only. 2) ΔL_{interf} is equal to the FWHM of the FT^{-1}[$|\underline{I}(\tilde{\nu})|$] = FT^{-1}[$|A(g(\tilde{\nu}))|$] profile (Fig. 6). In this case, the axial resolution depends on a combination of factors including the spectrum shape of the source, polarization effects and injection coupling in fibers that exhibits spectral behavior due to chromatic aberrations. Not all spectral components under the optical source envelope contribute to interference, and therefore ΔL_{interf} is expected to be larger than ΔL_{DC}. ΔL_{interf} is defined as the *achievable* experimental resolution of the interferometer. In practice, ΔL_{interf} is obtained by selecting one of the CS_{exp}, $I(\tilde{\nu})$, calculating its complex form $\underline{I}(\tilde{\nu})$ by using Appendix C, and Fourier transforming the absolute value $|\underline{I}(\tilde{\nu})|$.

As shown in Table 1, the resolution of CMSI is equal to the experimental resolution of the interferometer for the three peaks, ΔL_{interf}, which confirms our theoretical approach.

Table 1. Axial resolution according to the position of the reference mirror M in Fig. 1 (determining the optical path difference value) and the numerical tool used. ΔL_{DC} is the width of the peak FT^{-1}[$I_{DC}(g(\tilde{\nu}))$]. ΔL_{interf} is the width of the peak FT^{-1}[$|\underline{I}(\tilde{\nu})|$]. All widths are evaluated via a Gaussian fit.

	ΔL_{DC} (μm)	ΔL_{interf} (μm)	FT (μm)	CMSI (μm)
Position 1 240 μm	26±1	27.0±0.7	28.0±0.3	27.0±0.2
Position 2 740 μm	26±1	27.0±0.7	56.0±0.4	27.0±0.2
Position 3 1340 μm	26±1	26.1±0.7	104.5±0.9	26.2±0.2

MSI and CMSI are not sensitive to the deviation of the channeled spectrum modulation from a regular periodicity modulation [19], *i.e.* to the chirp coming from the nonlinearity of the decoder and from the unbalanced dispersion of the interferometer. Therefore there is no need for any compensation procedure as data resampling employed in the conventional FT based OCT practice.

5.3 A-scan with a swept source-based OCT without k-clock

The experimental set-up is similar to that presented in [15,17,18,20,21], where a swept source (Axsun Technologies, Billerica, MA), central wavelength 1060 nm, sweeping range 106 nm (quoted at 10 dB) and 100 kHz line rate is used. The interferometric signal from a balance detection receiver (Thorlabs, Newton, New Jersey, model PDB460C) is sent to one of the two inputs of a dual input digitizer (Alazartech, Quebec, Canada, model ATS9350, 500 MB/s). Although the SS used for our experiments was equipped with a k-clock, to fully demonstrate the benefits of the MSI, we did not take advantage of this facility. At the Master stage, three sets of P-channeled spectra CS_{exp} have been recorded, $P = 2$, $P = 11$ and $P = 491$, from $z = 143$ µm to $z = 2833$ µm.
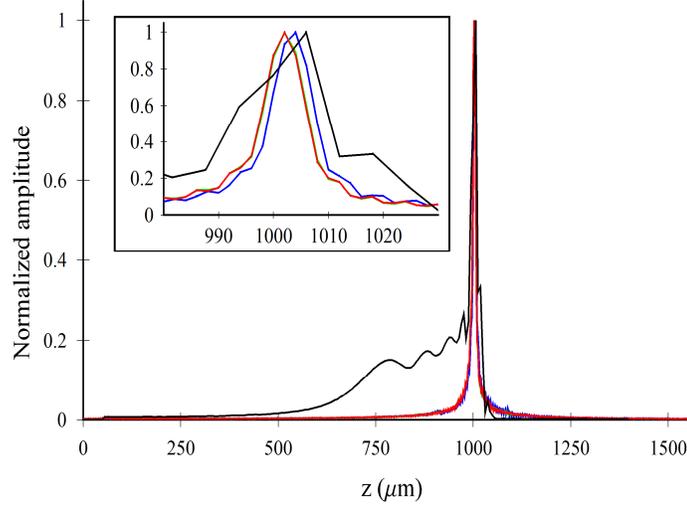
Fig. 7. A-scan for $z = 1001$ µm. Black line, A scan obtained with FT. The other three graphs are A-scan peaks obtained using the CMSI method with $Q = 776$, evaluated from different numbers of P-CS_{exp} used at the Master stage. Blue line, $P = 2$. Green line, $P = 11$. Red line, $P = 491$. Inset, details of the A-scans from 980 µm to 1030 µm.

At the Slave stage, a channeled spectrum has been recorded for a reference mirror positioned at 1001 µm measured from OPD = 0. Figure 7 shows the reflectance profile in depth based on Fourier Transform (black line) and on the CMSI method according to the three sets of CS_{exp} (blue line for $P = 2$, green line for $P = 11$ and red line for $P = 491$). Here again the Fourier transformation of the channeled spectrum corresponding to the reference mirror positioned at 1001 µm is calculated to demonstrate the existence of chirp in the channeled spectrum.

A depth sampling interval of 2 µm was chosen for CMSI to perform good sampling of the A-scan peaks, *i.e.* using $Q = 776$ masks for the range [0, 1550 µm]. The FT peak broadens due to the non-linearity of sweeping, as expected. The *achievable* experimental resolution of the interferometer ΔL_{interf} is equal to the FWHM of the $FT^{-1}[|\underline{I}(\tilde{v})|] = FT^{-1}[|A(g(\tilde{v}))|]$ profile, which is estimated to be 9.0±0.2 µm (Fig. 8) for the three sets of P-CS_{exp}. Lastly, in the inset of Fig. 7, the reflectance profiles are identical for $P = 11$ and $P = 491$, i.e. the green line overlaps the red line. For $P = 2$ (blue line), the A-scan displays a similar resolution but presents a slight shift of 2 µm and more noise on the edge of the peak.
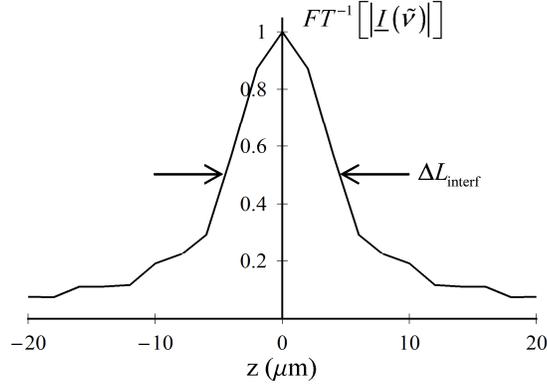
Fig. 8. PSF corresponding to the channeled spectrum I for an OPD = $2z$, where z = 1001 µm. The complex form $\underline{I}$ has been calculated in Appendix C. $FT^{-1}[|\underline{I}(\tilde{v})|]$ corresponds to the Fourier transformation of a channeled spectrum with no chirp.

5.4 Stability study and signal drop-off in depth: comparison between MSI and CMSI

In order to illustrate the insensitivity of CMSI to the random phase shift of channeled spectra acquired at the Master stage, several A-scans have been recorded over time while imaging a flat mirror. The interferometer used in this experiment is the same as in Section 5.3, *i.e.* a swept source without k-clock. The sampling in depth is chosen equal to 0.4 µm, much denser than the sampling obtained with the FT based method, estimated at 6.1 µm by measuring the displacement of the peak in Fourier domain according to the displacement of the reference mirror. This massive oversampling is implemented in order to determine a well-defined reflectance profile, to accurately measure the peak width (9.0±0.2 µm here).

The MSI signal has been calculated using Eq. (6) on data collected every 2 seconds and displayed in Fig. 9(a). To perform the calculation, 100 CS_{exp} have been recorded at the Master stage from OPD = 500 µm to 540 µm. These 100 CS_{exp} are used as masks. As shown in Fig. 9(a) and by the corresponding reflectance profile for a particular time in Fig. 9(c), the reflectance profiles are noisy. We interpret this as result of fluctuations in the phase of the channeled spectrum collected during measurement (Slave stage) combined with much larger phase fluctuations cumulated during the acquisition of the CS_{exp} channeled spectra during the Master stage.

In Fig. 9(b), the absolute value of CMSI signal has been calculated from the same raw data previously used for the MSI. To perform the calculation, the Mask function M_{built} has been calculated using P = 2 CS_{exp} measured at OPD = 500 µm and 540 µm and used to generate Q = 100 masks distanced at 0.4 µm. As shown in Fig. 9(b) and by the blue profile in Fig. 9(c) the CMSI reflectance profiles do not present significant fluctuations. This demonstrates the superiority of using masks generated theoretically, deprived from the random phase affecting the phase of experimentally collected channeled spectra. More quantification of this behavior represents the subject of future more rigorous experiments, for the limited study here we evaluated that the standard deviation of the random phase shift in the set-up was 0.27 rad per second. This still affects the resulting image in Fig. 9(b).
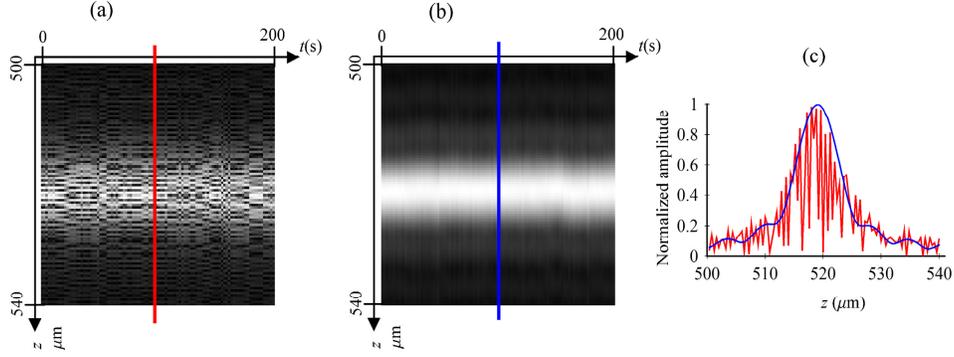
Fig. 9. (a) A-scans (vertical axis) for a mirror as object, represented in time (horizontal axis) calculated with MSI and $P = 100$ CS_{exp} utilized as masks. (b) A-scans (vertical axis) for a mirror as object represented in time (horizontal axis) calculated with CMSI using $Q = 100$ masks obtained from $P = 2$ CS_{exp}. (c) Reflectance profiles calculated by MSI (red) and CMSI (blue) for $t = 100$ s in each respective image.

Another important parameter to be compared between MSI and CMSI is the signal drop-off with optical path difference. To illustrate this, B-scans of the anterior chamber of a human eye have been obtained using CMSI (Fig. 10(a)) and MSI (Fig. 10(b)). The interferometer used in this experiment is the same as in Section 5.3, *i.e.* a swept source without k-clock. The sampling interval in depth is chosen equal to 5 μm. Both images are normalized to 1 according to the maximum of each of them.
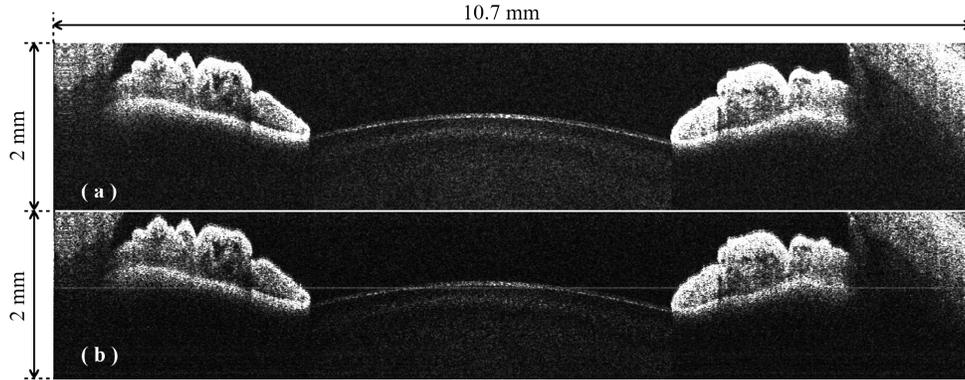
Fig. 10. (a) B-scan of the lens and the iris of a human eye with CMSI. (b) B-scan of the same raw data as in (a) but with MSI. Both images are normalized according to the maximum of each of them. To demonstrate the slight improvement in contrast at large depths of the CMSI image, we display their bottom only, showing the lens and the iris. The 2 mm-axial range of the B-scans is considered in air.

The sensitivity for both MSI and CMSI is measured as 101.3 dB close to OPD = 0 with a power equal to 1.7 mW on the sample, using the procedure detailed in [15]. The images are quite similar except for the drop-off in depth that is slightly larger for the MSI than for the CMSI. This is because in previous reports [15-21], MSI was implemented using the product between the raw channelled spectra and experimental masks, all affected by a decrease in their interference contrast with OPD. In CMSI, all masks have the same amplitude, hence an improvement in the decay of sensitivity with depth. This improvement can only be seen at large depths, therefore we have truncated the images to display large OPD values only, where

some improvement can be seen in the CMSI image. The expected improvement is anticipated by the difference between Eqs. (16b) and (25).

6. Conclusions

CMSI employs a Mask function to generate any number Q of masks, where each mask is used in the second stage, Slave measurement, to obtain the reflectivity of the object from a selected depth, characteristic for each mask. In previous implementations of MSI, the only depths addressed were those for which CS_{exp} were initially acquired at the Master stage. CMSI can create any number of intermediate masks between the depths where CS_{exp} were initially acquired from. This represents a major improvement in comparison with the implementations in [15-21], as CMSI requires fewer experimental measurements while allowing for much denser sampling in depth. This feature is especially important for high axial resolution OCT, where a large number of masks are needed to accurately construct an A-scan.

As with the correlation-based MSI method, there is no need for organizing the data in equally spaced frequency slots. The Mask function incorporates both the non-linearity of reading the channeled spectrum as well as the dispersion of the interferometer in the same way as the experimentally collected masks in the MSI Therefore, MSI and CMSI can work directly in the non-uniform distribution $\tilde{\nu}$ space in opposition to the conventional FT based spectral (Fourier) domain systems. In addition, as demonstrated here, CMSI can reach the expected theoretical resolution. MSI could equally achieve such resolution if the spectral envelope imprinted by the optical source spectrum is eliminated, procedure much improved in the CMSI, as shown in building Mask functions in Fig. 2. In the FT based OCT, achieving the best axial resolution depends on how good the resampling/linearization method is. Several methods have been developed to address this issue that allowed FT-based OCT methods to achieve axial resolutions close to the theoretical axial resolution. However, these procedures are performed in the very moment of data acquisition before displaying the results, involve extra computation resources and are time consuming. In MSI and CMSI the experimental masks and respectively the Mask function and derived masks are obtained at the Master stage, *i.e.* prior to measurement. The Master stage procedure can be considered as the equivalent to the resampling/linearization procedure in the FT-based OCT method. However, MSI and CMSI are radically different in output from the FT-based OCT methods. MSI and CMSI perform a procedure for each depth of interest while the FT-based methods deliver a full A-scan in a single step. Although this may look disadvantageous, MSI and CMSI allow a more direct production of *en-face* views, as there is no need, like in FT-based OCT method, to split the A-scan into its depth components.

In terms of time required by the CMSI in comparison with the MSI method, the main gain is at the Master Stage. While MSI would have required a tedious repetition of experimental collection of hundreds of channelled spectra subsequently used as masks, the CMSI presented here requires a much reduced number of channelled spectra to be experimentally collected at the Master stage, which can then be processed theoretically into as many masks needed.

In terms of calculation at the Slave stage, the only difference is that CMSI requires the operator for the core operation [21] to be implemented in complex, so the calculations at the Slave stage for the same number of masks require slightly more than the double the time of the MSI. This disadvantage may be eliminated by using graphic cards [18]. In terms of comparison of the time required by the core operator of the MSI with the time required by conventional FT based method, with or without resampling, this is benchmarked in Fig. 3 in [21]. Similarly, the improvement in the timing of the core operation using graphic cards detailed in [18] for the MSI can be extrapolated here for the CMSI method.

Finally, it has been shown that the theoretical expression for the operation of the CMSI is identical to the Fourier transform of channeled spectra for a perfect interferometer (no

dispersion) and perfect decoder, such as either a spectrometer linear in wavenumber or a linearly tunable swept source, however with the difference that the CMSI delivers a complex signal without random phase shift. This allows CMSI to eliminate the process of window integration practiced in the MSI, integration that has lead to worsening the axial resolution. Having access to the phase, CMSI method can be further explored to measure the phase of signal acquired from the object. The recovery of phase has not been employed here, however it is expected that this will trigger future developments in polarization and flow measurements.

7. Appendix A: demonstration of Eq. (4)

Let the Fourier transform (FT) and its inverse (FT^{-1}) be defined by the following expressions

$$FT\left[\hat{f}(t)\right] = \int \hat{f}(t)\,Exp\left[i\,2\pi\,t\,v\right]dt\,, \tag{28}$$

$$FT^{-1}\left[f(v)\right] = \int f(v)\,Exp\left[-i\,2\pi\,t\,v\right]dv\,. \tag{29}$$

The decoder is considered linear ($g(\tilde{v}) = \tilde{v} = v$) and the interferometer perfectly balanced for dispersion ($d \equiv 0$). According to (28), the inverse Fourier transform of I in (2), denoted as $\hat{I}$, is equal to

$$\hat{I}(t) = \hat{I}_{DC}(t) + \frac{1}{2}\hat{\underline{I}}(t) + \frac{1}{2}\hat{\underline{I}}(-t)^*\,, \tag{30}$$

where $\hat{I}_{DC}$ and $\hat{\underline{I}}$ are the inverse FT of I_{DC} and $\underline{I}$, and where for the last term the usual property of the Fourier transform was used

$$FT^{-1}\left[f(v)^*\right] = \hat{f}(-t)^*\,. \tag{31}$$

Eq. (30) can be evaluated for $t = 2z/c$ and becomes

$$\hat{I}(2z/c) = \hat{I}_{DC}(2z/c) + \frac{1}{2}\hat{\underline{I}}(2z/c) + \frac{1}{2}\hat{\underline{I}}(-2z/c)^*\,. \tag{32}$$

Moreover, for $g(\tilde{v}) = \tilde{v} = v$, Eq. (3) can be written as follows

$$\underline{I}(v) = \int r(\rho)\,A(v)\,Exp\left[i\,\frac{2\pi}{c}v\,2\rho\right]d\rho\,, \tag{33}$$

and its inverse FT evaluated for $t = 2z/c$ is equal to

$$\hat{\underline{I}}(t = 2z/c) = \iint r(\rho)\,A(v)\,Exp\left[-i\,\frac{2\pi}{c}v\,2(z-\rho)\right]d\rho\,dv\,, \tag{34}$$

that can be written as follows

$$\hat{\underline{I}}(2z/c) = \int \hat{A}\left(\frac{2}{c}(z-\rho)\right)r(\rho)\,d\rho = \hat{A}(2z/c)\otimes r(z)\,, \tag{35}$$

for which $\hat{A}(t) = FT^{-1}[A(v)]$.

8. Appendix B: demonstration of Eq. (10)

Eq. (9) can be written in the Fourier domain using a variable $\tilde{t}$, pair conjugate to $\tilde{v}$ as follows

$$MSI(z) = \frac{1}{2}\alpha(z)\,e^{-i\varphi_{rand}(z)}\int \underline{\square CS}(\tilde{t},z)^*\,\hat{I}(\tilde{t})\,d\tilde{t} + CC\,, \tag{36}$$

by using the Plancherel-Parceval theorem defined by

$$\int f_1^*(\tilde{v})\,f_2(\tilde{v})\,d\tilde{v} = \int \hat{f}_1^*(\tilde{t})\,\hat{f}_2(\tilde{t})\,d\tilde{t}\,, \tag{37}$$

for which $f_1 = FT\left[\hat{f}_1\right]$ and $f_2 = FT\left[\hat{f}_2\right]$.

Similar to (30), the inverse Fourier transform of the channeled spectrum I is equal to

$$\hat{I}(\tilde{t}) = \hat{I}_{DC}(\tilde{t}) + \frac{1}{2}\underline{\hat{I}}(\tilde{t}) + \frac{1}{2}\underline{\hat{I}}(-\tilde{t})^{*}.$$ (38)

For an object placed axially in respect to the OCT system, in such a way as the OPD = 0 is placed outside of the object, the product $\underline{\hat{CS}}^{*} \times \hat{I}$ is only equal to $1/2\,\underline{\hat{CS}}^{*} \times \underline{\hat{I}}$. Indeed the position of the peak $\underline{\hat{CS}}$ depends on z that is defined for $z>2L_c$ only, condition that avoids the peak $\underline{\hat{CS}}$ to overlap the peak $\hat{I}_{DC}$ (see Fig. 11).
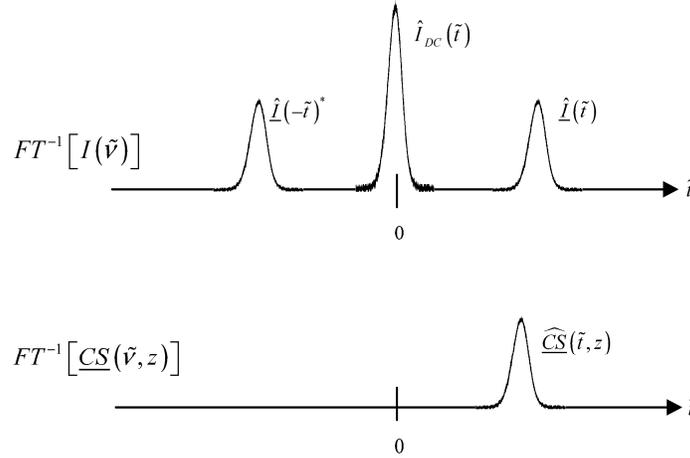
Fig. 11. Schematic representation of the peaks obtained by calculating the inverse FT of I (top) and $\underline{CS}$ (bottom) for a single layer object. The OPD is chosen so that $\underline{\hat{I}}$ does not overlap $\hat{I}_{DC}$.

Then we have

$$\int \underline{\hat{CS}}(\tilde{t},z)^{*}\,\hat{I}(\tilde{t})d\tilde{t} = \frac{1}{2}\int \underline{\hat{CS}}(\tilde{t},z)^{*}\,\underline{\hat{I}}(\tilde{t})d\tilde{t}.$$ (39)

By using the Plancherel-Parseval theorem, Eq. (39) is written as follows

$$\int \underline{\hat{CS}}(\tilde{t},z)^{*}\,\hat{I}(\tilde{t})d\tilde{t} = \frac{1}{2}\int \underline{CS}(\tilde{v},z)^{*}\,\underline{I}(\tilde{v})d\tilde{v},$$ (40)

and the expression of MSI(z) is equal to

$$MSI(z) = \frac{1}{2}\alpha(z)\Re e\left\{ e^{-i\varphi_{rand(z)}} \int \underline{CS}(\tilde{v},z)^{*}\,\underline{I}(\tilde{v})d\tilde{v} \right\},$$ (41)

where Re{} means the real part of a complex function.

9. Appendix C: complex exponential form of a real sinusoidal function

Let $f(v)$ be a real sinusoidal function modulated at a and defined by the following expression

$$f(v) = I_{DC}(v) + \frac{1}{2}\underline{I}(v)e^{ia2\pi v} + \frac{1}{2}\underline{I}(v)^{*}e^{-ia2\pi v}.$$ (42)

The complex form $\underline{f}(v)$ of $f(v)$ is then equal to $\underline{I}(v)e^{ia2\pi v}$ and can be retrieved using (29) and the steps shown in Fig. 12.

$$f(\nu)=I_{DC}(\nu)+\frac{1}{2}\underline{I}(\nu)e^{i2\pi\nu a}+\frac{1}{2}I(\nu)^{*}e^{-i2\pi\nu a} \xrightarrow{\ \text{FT}^{-1}\ } \hat{f}(t)=\hat{I}_{DC}(t)+\frac{1}{2}\hat{\underline{I}}(t-a)+\frac{1}{2}\hat{\underline{I}}(-t-a)^{*}$$

$$\underline{f}(\nu)=\underline{I}(\nu)e^{i2\pi\nu a} \xleftarrow{\ \text{FT}\ } \hat{f}(t)G(t)=\hat{\underline{I}}(t-a)$$

$$\times G(t)=\begin{cases} 0 & if\ t<t_{0} \\ 2 & if\ t>t_{0} \end{cases}$$
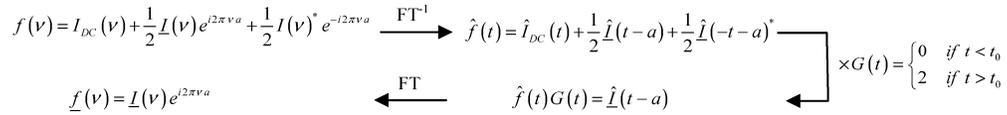
Fig. 12. Diagram explaining the process of changing a real sinusoidal function into a complex form. The parameter t_0 is chosen to eliminate the DC component of the real sinusoidal function.

10. Appendix D: demonstration of Eq. (22)

Eq. (22) can be written in the Fourier domain by using the Plancherel-Parseval theorem as follows

$$CMSI(z)=\int \hat{M}_{built}(\tilde{t},z)^{*}\,\hat{I}(\tilde{t})\,d\tilde{t}\ . \tag{43}$$

For an OPD = 0 placed outside of the object, only the product $1/2\,\hat{M}_{built}{}^{*}\times\hat{\underline{I}}$ is different from 0, according to similar reasoning used in Fig. 10 in Appendix B. Therefore, the CMSI signal can be written, after using the Plancherel-Parseval theorem, as follows

$$CMSI(z)=\frac{1}{2}\int M_{built}(\tilde{\nu},z)^{*}\,\underline{I}(\tilde{\nu})\,d\tilde{\nu}\ . \tag{44}$$